Journal of Materials Chemistry A

ROYAL SOCIETY OF CHEMISTRY

PAPER

View Article Online
View Journal | View Issue

Cite this: *J. Mater. Chem. A*, 2024, **12**, 20935

Sodium 4-styrenesulfonyl(trifluoromethane sulfonyl)imide-based single-ion conducting polymer electrolyte incorporating molecular transporters for quasi-solid-state sodium batteries†

Clemens Wunder,[ab] Thanh-Loan Lai,[cd] Edina Šić,[e] Torsten Gutmann,[e] Eric De Vito,[cd] Gerd Buntkowsky,[e] Maider Zarrabeitia *[ab] and Stefano Passerini *[ab]

Sodium batteries are an attractive alternative for future energy storage as they can be produced with abundant and low-cost materials. Nonetheless, sodium-ion batteries (SIBs) are often composed of flammable and volatile carbonate-based liquid electrolytes. Polymer electrolytes have attracted significant attention as safer alternatives. Among polymer electrolytes, single-ion conductive polymer electrolytes (SIPEs) are considered particularly interesting because they can suppress dendrite growth, enabling high-performance (quasi)-solid-state sodium–(metal) batteries. In this work, a self-standing, flexible, quasi-solid-state SIPE is investigated, which is composed of sodium 4-styrene sulfonyl (trifluoromethanesulfonyl) imide (NaSTFSI), pentaerythritol tetrakis(3-mercaptopropionate) (PETMP) and pentaerythritol tetraacrylate (PET4A) blended with poly(vinylidene fluoride-*co*-hexafluoropropylene) (PVDF-HFP). The SIPE membrane, including 50 wt% of molecular transporter, exhibits ionic conductivity of 1.4×10^{-5} S cm^{-1} and 1.3×10^{-4} S cm^{-1} at 20 °C and 90 °C, respectively, thermal stability up to 280 °C, electrochemical stability window up to 4.5 V *vs.* Na/Na$^+$, and Na plating/stripping reversibility in symmetric Na||Na cells. The manufactured SIPE implemented in Prussian White (PW)||Na cells enables the delivery of 147 mA h g^{-1} of PW at 15 mA g^{-1} with a Coulombic efficiency of over 99%, which is comparable with the PW||Na cells using liquid carbonate electrolyte, confirming the suitability of the designed SIPE for sodium–(metal) batteries.

Received 5th April 2024
Accepted 11th July 2024

DOI: 10.1039/d4ta02329c

rsc.li/materials-a

[a]*Helmholtz Institute Ulm (HIU), Helmholtzstrasse 11, D-89081 Ulm, Germany*
[b]*Karlsruhe Institute of Technology (KIT), P.O. Box 3640, D-76021 Karlsruhe, Germany*
[c]*University Grenoble Alpes, F-38054 Grenoble, France*
[d]*CEA, LITEN, F-38054 Grenoble, France*
[e]*Technical University of Darmstadt, Institute for Inorganic and Physical Chemistry, Peter-Grünberg-Straße 8, D-64287 Darmstadt, Germany. E-mail: maider.ipina@kit.edu; stefano.passerini@kit.edu*

† Electronic supplementary information (ESI) available. See DOI: https://doi.org/10.1039/d4ta02329c

Maider Zarrabeitia

Dr Maider Zarrabeitia is associated principal investigator and group leader of Beyond Li: materials and interphases groups at Helmholtz-Institute Ulm (HIU) since 2022. Her activities focuses on electrode materials and electrolytes beyond lithium-based technology, such as sodium- and potassium-based batteries, as well as the understanding of electrode–electrolyte interphases for several battery technologies. She received her Ph.D. in Materials Science and Technology in 2016 from the University of Basque Country (UPV/EHU, Spain) while being a researcher of CIC energiGUNE, including two research stages at the University of Camerino (Italy). She is a principal investigator of several national and international competitive research projects, and author of >50 articles published in international high-impact journals, with >1500 citations, and co-author of 1 book chapter.

Introduction

The growing demand for lithium-ion batteries (LIBs) guides attention toward more sustainable and lower cost energy storage devices. The most promising candidates are SIBs.[1] Sodium is abundant worldwide and relatively cheap to extract, while sustainable materials can be used as positive and negative electrodes. Indeed, SIBs offer comparable performance to $LiFePO_4$-based LIBs and are already on the market for light electric vehicles and large-scale applications.[2] Several companies can manufacture SIBs, such as Contemporary Amperex Technology Co., Ltd. (CATL), Build Your Dreams (BYD), HiNa, and Faradion, employing layered oxides as the positive electrode (cathode) and hard carbon as the negative electrode (anode). Meanwhile, the cooperation between Altris and Northvolt focuses on commercializing low-cost SIBs with PW as the cathode material. PW is produced from non-toxic, globally abundant, and low-cost raw materials and thus is a promising candidate for large-scale energy storage.[3] Overall, SIB's production is expected to grow up to 186 GW h per year by 2030, which would be enough energy to power 4.6 million electric vehicles per year.[4,5]

LIBs and SIBs share the use of electrolytes based on organic solvents, exhibiting high ionic conductivity, but are also toxic, volatile, and flammable, raising serious safety issues. Solid-state batteries (SSBs) are safer and greener and have a reduced risk of thermal runaway or short circuit through dendrite formation. Moreover, SSBs may provide higher energy density than liquid electrolyte-based SIBs due to the possibility of using sodium metal as the negative electrode,[6] which allows a compact and light design.[1,7,8] Depending on their chemistry, solid-state electrolytes (SSEs) can be divided into three main groups, *i.e.*, inorganic glass/ceramics, organic polymers, and hybrid composites.[9] Organic polymer electrolytes, however, stand out through their self-standing properties, reliability, and modularity. They strive for good ionic conductivities at room temperature (RT) while offering good thermal and mechanical stability. Furthermore, a wide electrochemical window and no side reactions with the electrodes are desired for high-performing SSBs. Nevertheless, it should be noted that organic polymer electrolytes usually suffer from poor oxidation stability.[10]

The most common organic polymer electrolytes are based on neutral polymers, such as polyethylene oxide (PEO),[11] polymethyl methacrylate (PMMA),[12] or polyacrylonitrile (PAN),[13] which provide long flexible chains with negatively charged groups that can interact with sodium salts, *e.g.*, $NaPF_6$, NaFSI or NaTFSI, to form a polymer–salt complex.[14] These organic polymer electrolytes, however, exhibit low ionic conductivity at RT because the Na^+ ion mobility is strongly bound to the polymer chains' mobility. Therefore, they are usually swollen with organic carbonate solvents, forming gel polymer electrolytes, or doped with ceramics to form composite polymer electrolytes to improve ionic conductivity at RT.[15–17] Since the Na salt ions are free in the polymer matrix, concentration gradients occur during cycling, especially at high charge/discharge rates. The sodium concentration gradient, further increasing over time due to the counteracting anion concentration gradient,[18,19] results in non-uniform Na plating and dendrite growth, leading to severe safety issues through the risk of short circuits.[20]

SIPEs avert the concentration gradient issue by anchoring the anion to the polymeric backbone, also allowing the transference number of the Na^+ cation to reach nearly unity.[14,20–22] The desired SIPEs possess high ionic conductivity, thermal stability, mechanical strength, high ion transference number, and a wide electrochemical window while being of low-cost.[20] A few sodium-based SIPEs have been reported for sodium–(metal) batteries so far. The most common SIPEs are based on sodium salt monomers containing a $TFSI^-$ anion, such as poly(sodium 1-[3-(methacryloyloxy)propylsulfonyl]-1-(trifluoromethanesulfonyl) imide) (PNaMTFSI)[23] and sodium multi-block ionomer.[10] PNaMTFSI is blended with PEO to exhibit ionic conductivities of 7.7×10^{-5} S cm^{-1} at 85 °C, while the sodium multi-block ionomer has a fluorinated backbone and a modified TFSI sidechain to reach 2.0×10^{-3} S cm^{-1} at RT. Additionally to TFSI-based SIPEs, other sodium salt monomers, such as borates-based SIPEs, are under investigation. Sodium–poly(tartaric acid)borate (NaPTAB)[24] achieves an ionic conductivity of 9.4×10^{-5} S cm^{-1} at RT. Sodium bis(fluoroallyl)malonato borate salt (NaBFMB), which is co-polymerized to form a 3-D cross-linked network, reaches high ionic conductivity of 2.0×10^{-3} S cm^{-1} at 30 °C. Moreover, the poly(sulfamate-carboxylate) (PICS) SIPE delivers 1.8×10^{-5} S cm^{-1} at RT by using sulfonate and carbonate as counter-anion.[25] However, the ionic conductivity of sodium-based SIPEs still needs to be enhanced to become competitive with liquid or gel polymer electrolytes.

In this work, a three-dimensionally (3D) structured SIPE has been designed (ESI, Fig. S1†) composed of PETMP and PET4A monomers and in-house synthesized TFSI-based sodium salt monomer (NaSTFSI), offering great charge delocalization for the Na^+ ion conduction. The mechanical properties of the manufactured SIPE membrane (herein referred to as NaSTFSI-*co*-PET-MP/4A) have been further improved by blending with PVDF-HFP polymer. The NaSTFSI-*co*-PET-MP/4A electrolyte containing 50 wt% of molecular transporters shows good sodium ionic conductivity and a wide electrochemical stability window. As a proof of concept, PW‖Na quasi-solid-state sodium–metal cell has been assembled, delivering similar capacity, Coulombic efficiency, and capacity retention to the PW‖Na cell containing organic liquid electrolyte at 40 °C.

Experimental section

Synthesis of NaSTFSI monomer

NaSTFSI was synthesized using a two-step synthesis route (ESI, Fig. S2†).[26] A solution of thionylchloride (44 mL, 606.54 mmol, Thermo Scientific, 99.7%) in dry dimethylformamide (DMF, 200 mL, VWR chemicals, 99.8%) was prepared under Ar atmosphere by stirring both components together for 3 h at RT. The solution was cooled before adding the inhibitor 4-*tert*-butylcatechol (600 mg, 3609.74 mmol, Sigma-Aldrich, >99%) followed by the slow addition of the educt sodium 4-vinylbenzenesulfonate (NaVBS, 16 g, 77,59 mmol, Sigma-Aldrich, >90%). The solution

was stirred for 16 h at RT and cooled in the fridge at 4 °C for 24 h. The obtained solution was slowly dropped into an ice-cooled solution of water (100 mL) and dichloromethane (DCM, 100 mL, VWR chemicals, >99%). The DCM phase was collected, while the water phase was washed twice with DCM (2 × 50 mL). The DCM phases (NaVBSC, see ESI, Fig. S2†) were combined and the solvent was removed in vacuum at 50 °C and the residue was cooled before adding acetonitrile (120 mL, VWR chemicals), trifluoromethanesulfonamide (15 g, 53.35 mmol, Thermo Scientific, 96%) and triethylamine (200 mL, VWR chemicals, >99%). The solution was stirred for 72 h, filtered, and the solvent was removed at 50 °C under reduced pressure. DCM (100 mL) was added to the obtained solution before being washed with cooled water (2 × 50 mL). The DCM phases were combined, and the solvent was evaporated at 50 °C under reduced pressure. Sodium carbonate (18 g, Sigma Aldrich, ≥99.5%) and dry methanol (100 mL) were added before the solution was stirred for 24 h at RT. The precipitate was removed using a centrifuge, and the solvent was evaporated. The resulting precipitate was washed twice with acetone (25 mL) and dried in air to obtain NaSTFSI (4.2 g, yield = 17%) as an off-white solid powder.

NaSTFSI-*co*-PET-MP/4A membrane fabrication

NaSTFSI-*co*-PET-MP/4A membranes were prepared by solvent casting using dimethyl sulfoxide (DMSO, VWR chemicals, >99%) and DMF (VWR chemicals, 99.8%) mixture. First, the two networking monomers PETMP (500 mg, Merck, 97%) and PET4A (200 mg, VWR Merck, 99%) were dissolved together with PVDF-HFP (80 mg, Merck) in DMF (9 mL). In contrast, the NaSTFSI sodium salt monomer (70 mg) was dissolved in DMSO (3 mL) together with the thermal initiator azobisisobutyronitrile (AIBN, 9 mg, Merck, 98%). The two solutions were first stirred separately for 3 h, then mixed and stirred for an additional 2 h, and, finally, cast into a Teflon Petri disk (62 mm Ø). The solution was covered with a perforated Al foil and heated to 70 °C for 28 h, while the pressure was stepwise reduced to 10 mbar. This procedure resulted in self-standing NaSTFSI-*co*-PET-MP/4A membranes of 140 ± 40 μm. The NaSTFSI-*co*-PET-MP/4A membranes were cut into round discs (16 mm Ø) and further dried at 70 °C in vacuum for 3 h. The membranes were transferred in a glovebox (O_2 < 0.1 ppm, H_2O < 0.1 ppm) and swollen in a mixture of ethylene carbonate (Aldrich, 99%), dimethyl carbonate (Aldrich, 99.9%) and fluoroethylene carbonate (Aldrich, 99%) (EC : DMC : FEC, 49 : 49 : 2, vol%) (2 mL), at 60 °C for 48 h before they were used in a sodium–metal cells (no liquid leaking was observed). The solvent uptake was 50 ± 4 wt%, which corresponds to the maximum amount of molecular transporter uptaken by the NaSTFSI-*co*-PET-MP/4A membrane without any evident liquid leaking.

Physicochemical and thermal characterization

The structure of NaSTFSI was investigated by liquid nuclear magnetic resonance (^{1}H-, ^{13}C-, and ^{19}F-NMR) using an NMR spectrometer (Bruker Avance 400, ^{1}H at 400 MHz). DMSO-d6 was used as the solvent. ^{1}H → ^{13}C cross-polarization magic angle spinning (CPMAS) NMR experiments of NaSTFSI and NaSTFSI-*co*-PET-MP/4A were performed similarly to a previous report[27] on a Bruker Avance III HD 600 NMR spectrometer at 14.1 T operating at a frequency of 600.12 for ^{1}H and 150.92 MHz for ^{13}C. A 3.2 mm rotor was used to spin the samples at 10 kHz. For the ^{1}H → ^{13}C CPMAS spectra, a π/2 excitation pulse on ^{1}H was applied with a duration of 2.3 μs. A linear ramp (50–100) was used on the ^{1}H channel during cross-polarization transfer with a contact time of 2 ms. 512 scans were collected employing a repetition delay of 4 s, corresponding to 35 min of measurement time for each spectrum. For heteronuclear ^{1}H decoupling, the ppm 15 sequence was applied during acquisition.[28] ^{13}C CPMAS NMR chemical shifts were referenced with respect to tetramethylsilane (TMS = 0 ppm) using glycine as an external standard (C=O signal at 176.5 ppm). The signal assignment was based on the ^{13}C NMR chemical shifts predicted from the chemical structure of NaSTFSI using the ACD Lab/NMR software. Fourier transform infrared spectroscopy (FT-IR) was performed on an FT-IR spectrometer (Perkin Elmer Spectrum Two) between 400 and 4000 cm^{-1} to study the characteristic bonds in the synthesized monomer and NaSTFSI-*co*-PET-MP/4A membrane. Thermogravimetric analysis (TGA) coupled with mass spectroscopy (MS) was carried out on a Netzsch TG 209 F1 with a heating rate of 5 K min^{-1}. The NaSTFSI-*co*-PET-MP/4A membrane was sealed in Al crucibles and was measured between 30 and 600 °C using a sample mass of ∼5 mg, while a N_2 flow was used to collect and then measure the produced fractions during heating. Differential scanning calorimetry (DSC, Discovery series, T.A. Instruments) was performed on the NaSTFSI-*co*-PET-MP/4A membranes (∼10 mg in sealed Al pans) in three sweeps between −100 to 230 °C using a heating rate of 5 K min^{-1} under N_2 (gas flow: 10 mL min^{-1}).

Surface characterization

Surface chemistry of the NaSTFSI-*co*-PET-MP/4A samples before and after cycling was investigated by using a combination of X-ray photoelectron spectroscopy (XPS) and Time-of-Flight secondary ion mass spectrometry (ToF-SIMS). XPS analyses were achieved on a PHI Versaprobe II spectrometer. Charging effects were controlled during analysis with a combination of a low-energy electron gun (negative charge) and a low-energy argon gun (positive charge). The X-ray source was an Al Kα monochromatic beam (1486.7 eV), and the take-off angle was set at 45°. Pass energy was set to 23.5 eV for high-resolution spectral acquisition, providing an energy resolution of ∼0.6 eV. Data treatment was performed using the MultiPak software. Spectra were calibrated by using C 1s in C–C/C–H as a reference binding energy (at 284.8 eV). ToF-SIMS measurements were carried out with a ToF.SIMS.5 spectrometer (ION-TOF GmbH), equipped with a 30 kV Bi cluster primary-ion gun. High-resolution imaging analyses were performed in negative ion mode using Bi_3^+ (30 keV) as primary ion species for analysis with a primary ion current of ∼0.1 pA. Cycle time was set at 100 μs. Analysis was carried out in delayed extraction mode. Surface areas of 50 × 50 μm^2 were rasterized in random mode with 512 × 512 pixels, 1 shot per frame per pixel, and 1 frame per patch.

Measurements were stopped when the total count for total ions reached $\sim 10^7$ counts. During all measurements, charge compensation was applied with a low-energy electron flood gun. Evaluation of ToF-SIMS data was achieved with the software SurfaceLab 7.3.

Electrochemical characterization

The electrochemical properties of NaSTFSI-*co*-PET-MP/4A electrolyte were investigated in four different coin cell (S4R, CR2032) configurations employing: (i) two Al current collectors for ionic conductivity determination, (ii) two Na metal discs (12 mm, Merck, >99.9%) for stripping/plating tests and interfacial resistance analysis; (iii) Al current collector and a Na metal disc for linear sweep voltammetry (LSV), and (iv) PW electrode (Altris) and a Na metal disc as positive and negative electrodes, respectively, for galvanostatic tests. The coin cells were sealed using a hydraulic coin cell crimping machine (CR2032, S4R, pressure of ~800 psi). Electrochemical impedance spectroscopy (EIS) measurements were carried out with the Solartron SI 1260/1287 Impedance Analyzer (frequency range: 1 kHz to 1 MHz, amplitude: 10 mV) in the temperature range from 10 and 90 °C for ionic conductivity determination. The temperature was controlled using a Binder climatic chamber (KB23). The cell rested for 3 h after reaching a new temperature prior to measurement. The impedance response was analyzed using the RelaxIS 3 software with an R.P. fit. The ionic conductivity was calculated using the formula $\sigma = \frac{d}{RA}$, where σ is the ionic conductivity, R is the obtained resistance from the impedance measurements, and d and A are, respectively, the thickness (measured *ex situ* using a Mitutoyo Absolute digital thickness gauge 547–401) and the area of the NaSTFSI-*co*-PET-MP/4A electrolyte. A Biologic SAS VMP-3e was used to measure the stripping/plating behavior, the anodic/cathodic stability, and the interfacial resistance at 40 °C, storing the cells in a Binder climatic chamber KB23. In the stripping/plating tests, the current density was varied between 10 and 50 μA cm^{-2} and reversed every 1 h. EIS tests were conducted after 1 h of OCV and after 10 cycles at each current density. The LSV cells were rested for 6 h and later tested at a scan rate of 30 μV s^{-2}.

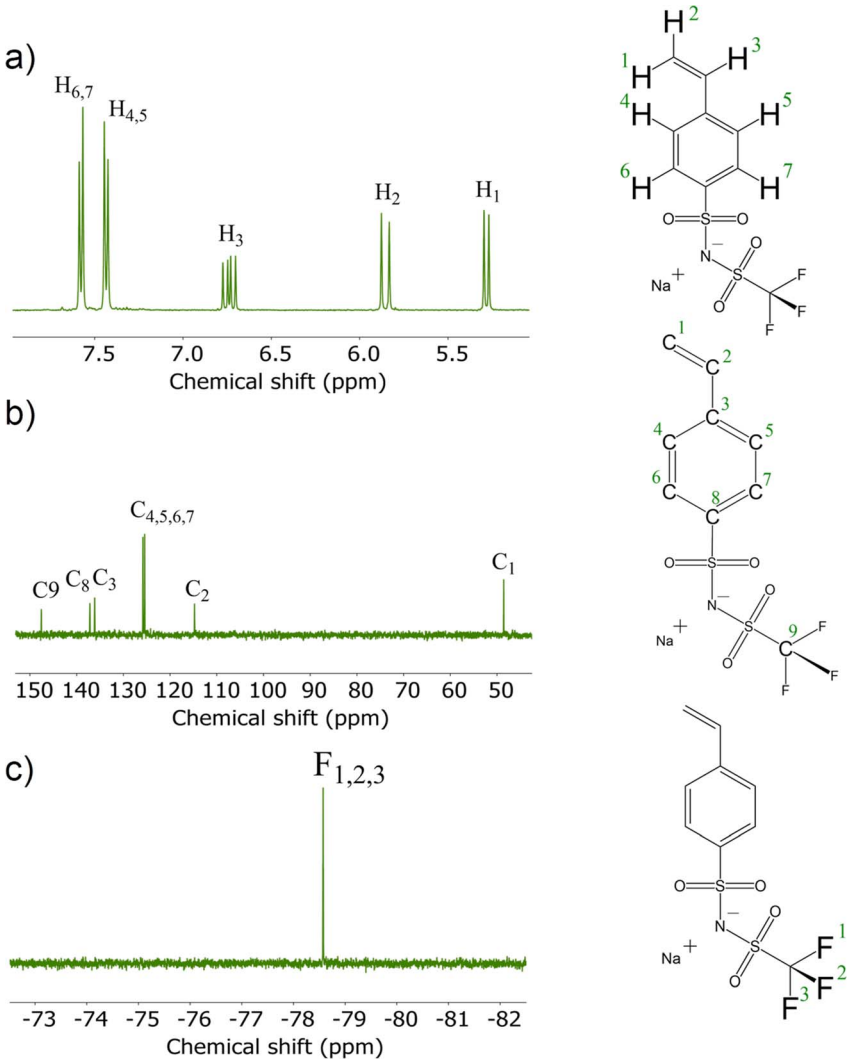

Fig. 1 (a) ^{1}H, (b) ^{13}C, and (c) ^{19}F-NMR spectra and structure of NaSTFSI sodium salt monomer.

The galvanostatic tests of rhombohedral PW, $Na_2Fe[Fe(CN)_6]$ from Altris, in Na cells were carried out at 40 °C (Binder climatic chamber KB 115) by using a Maccor 4000 battery testing system to apply a constant current (CC) of C/50 for the initial cycle followed by 5 cycles of C/20 and ongoing cycles of C/10 until failure (1C = 150 mA h g^{-1}). In addition, upon desodiation (charging), a constant voltage (CV) was applied at 3.8 V until a current density lower than 0.02C was reached. The cathode consisted of 80% PW (Altris), 10% carbon additive (Super P45), 5% carboxymethyl cellulose (CMC), and 5% styrene–butadiene rubber (SBR, Zeon) with a mass loading of 1.3 ± 0.4 mg cm^{-2}. The PW electrodes were dried at 70 °C at 10^{-7} mbar for 24 hours and stored in a glovebox (O_2 < 0.1 ppm, H_2O < 0.1 ppm).

Results and discussion

NaSTFSI sodium salt monomer and NaSTFSI-*co*-PET-MP/4A electrolyte characterization

To synthesize the ionic conducting SIPEs for (quasi)-solid-state sodium–(metal) batteries, a monomer carrying Na^+ ions was developed. The mobility of the Na^+ cation inversely depends on the binding strength toward the anion. This can be reduced by increasing the size of the anionic center since a delocalized negative charge results in a weak anionic strength towards the cation. Therefore, the designed sodium salt monomer was based on the bis(trifluoromethanesulfonyl)imide ($TFSI^-$) anionic center synthesized from NaVBS (ESI, Fig. S2†). The structure of the in-house synthesized NaSTFSI sodium salt monomer was verified using ^{1}H-, ^{13}C-, and ^{19}F-NMR spectroscopy (Fig. 1).[26] The ^{1}H-NMR shows the four benzyl proton doublets at 7.5 ppm, followed by the double doublet at 6.74 ppm. Last, the protons of the double bond are shown at 5.85 and 5.28 ppm as doublets, respectively. The ^{13}C-NMR shows all 9 carbon atoms between 110 and 150 ppm with the only exception of the terminal C of the double bond, which is shifted down to 50 ppm. Last, the ^{19}F-NMR shows all three fluor atoms at −79 ppm, which is in agreement with the literature.

The NaSTFSI-*co*-PET-MP/4A membrane (ESI, Fig. S1†) was manufactured by mixing the homemade NaSTFSI sodium salt monomer with PETMP, PET4A, and PVDF-HFP. The 3D network structure of the NaSTFSI-*co*-PET-MP/4A membrane could be confirmed through the creation of a new sulfur–carbon bond between PETMP and PET4A/NaSTFSI observed by combined FT-IR and NMR investigations as follows. Fig. 2a illustrates the FT-IR spectra of the three monomers, *i.e.*, NaSTFSI, PET4A, PETMP, and the NaSTFSI-*co*-PET-MP/4A membrane. The NaSTFSI shows the characteristic stretching peaks of C–H around 3065 cm^{-1}, C=C at 1630 cm^{-1}, SO_2 at 1237 cm^{-1}, S=O at 1045 and 1008 cm^{-1}, and aromatic C–H at 676 cm^{-1}, and deformation vibration of N–SO_2 at 1182 and 1129 cm^{-1} and =C–H at 991, 906 and 843 cm^{-1}, confirming the successful synthesis of the NaSTFSI sodium salt monomer, and in agreement with literature.[29,30] Meanwhile, the NaSTFSI-*co*-PET-MP/4A membrane shows characteristic features of the three monomers, such as the stretching peaks of C–H (2960 cm^{-1}), C=O (1728 cm^{-1}), C–O–C (1130 cm^{-1}) and C–O (1015 cm^{-1}) groups, as well as the CH_2 (1411 and 1346 cm^{-1}), C–H (952 cm^{-1}) and =C–H (880 cm^{-1}) deformation vibrations. Noteworthy, the FT-IR spectrum of the membrane is similar to that of PETMP due to its highest weight fraction. Moreover, the FT-IR spectrum of the NaSTFSI-*co*-PET-MP/4A membrane displays a new IR peak at 3400 cm^{-1}, corresponding to C–H bonds. However, the characteristic peak of the S–H group (2564 cm^{-1}) of PETMP vanished, suggesting the reaction of the S–H groups with free vinyl groups to form the new S–C bond, thus creating the proposed 3D NaSTFSI-*co*-PET-MP/4A structure (ESI, Fig. S1†).[31,32]

The ^{1}H → ^{13}C CPMAS NMR spectrum of NaSTFSI (Fig. 2b) exhibits overlapping resonances in the chemical shift range between 100 and 160 ppm, which contain spinning side-bands marked with asterisks. At least four different signals are distinguished, which overlay into a broad signal, probably referring to quaternary carbons in the aromatic ring. The signal at 115 ppm is attributed to the –CH_2 of the vinyl group. The signals at 128 and 138 ppm are originating from the carbons in the benzene ring. The signal at 143 ppm most probably refers to the –CH carbon of the vinyl group attached to the aromatic ring. Therefore, the ^{1}H → ^{13}C CPMAS NMR confirms once more the successful synthesis of NaSTFSI sodium salt monomer.

Significant changes are observed comparing the spectra of NaSTFSI (Fig. 2b) and NaSTFSI-*co*-PET-MP/4A (Fig. 2c). The NaSTFSI-*co*-PET-MP/4A shows signals at 41 and 171 ppm that do not refer to spinning side-bands. The asymmetric signal at

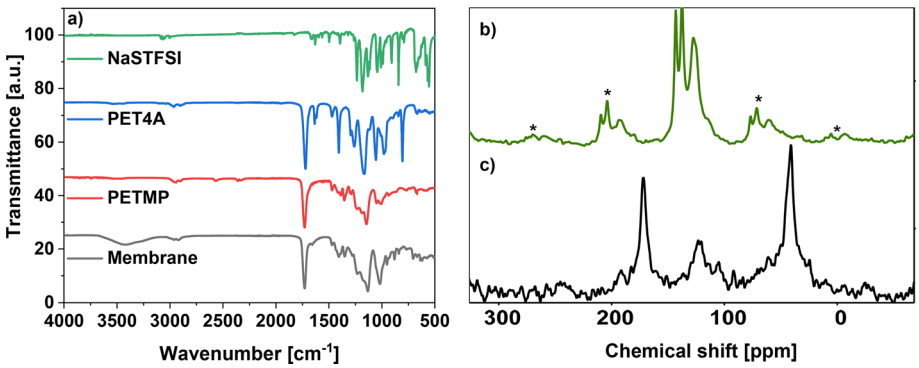

Fig. 2 (a) FT-IR spectra of NaSTFSI, PET4A, PETMP, and NaSTFSI-*co*-PET-MP/4A membrane. ^{1}H → ^{13}C CPMAS NMR spectrum of (b) NaSTFSI and (c) NaSTFSI-*co*-PET-MP/4A electrolyte, recorded at 10 kHz and 14.1 T. Note: Signals marked with asterisks (*) are spinning side-bands.

41 ppm is attributed to aliphatic species, whereas the narrow peak at 171 ppm is assigned to carbonyl groups (C=O) in the polymer network.[33] The line broadening makes it difficult to match the signals between 95 and 150 ppm to the different components. The resonances may originate from aromatic sp^2 carbons,[33] as well as from fluorine-containing moieties such as CF_2/CF_3 groups, according to the literature.[34,35] To prove this hypothesis, additional ssNMR measurements, including 2D techniques, have to be performed, which are beyond the scope of the present work. Nevertheless, the obtained results agree well with the FT-IR, suggesting the 3D structure of the NaSTFSI-*co*-PET-MP/4A SIPE.

Thermal properties of NaSTFSI-*co*-PET-MP/4A

The thermal stability of the NaSTFSI-*co*-PET-MP/4A membrane was investigated *via* TGA coupled with MS to identify the decomposition species. The NaSTFSI-*co*-PET-MP/4A membrane is stable up to 280 °C (black curve, Fig. 3a), which is comparable with other Na-based SIPEs.[10,25,36] The mass loss in the 130–280 °C range is negligible. The collected mass losses (colored curves in Fig. 3a) indicate the release of N_2 ($m/z = 28$), O_2 ($m/z = 32$), O ($m/z = 16$), and N ($m/z = 14$), probably associated to air bubbles trapped inside the NaSTFSI-*co*-PET-MP/4A membrane. At temperatures higher than 280 °C, a species with a mass of 19 is released, suggesting that fluorine is released upon membrane degradation.

The DSC measurement confirms the high thermal stability of the membrane, showing a minimal heat flow (below 1 mW) when heating up to 200 °C, down to −100 °C, and then up to 200 °C again. The increase in the heat flow at 20 °C corresponds to the membrane's glass transition temperature (T_g), which is in the same range as for the Li-based SIPE analogue.[30] In addition, the NaSTFSI-*co*-PET-MP/4A membrane exhibits a small peak (T_m) around 110 °C for the heating and cooling scan, related to the crystallization and melting temperature of the polymer membrane.[37,38]

Electrochemical characterization of NaSTFSI-*co*-PET-MP/4A electrolyte

The electrochemical properties of the SIPE, consisting of NaSTFSI-*co*-PET-MP/4A (50 wt%) impregnated with 50 wt% of EC : DMC : FEC (49 : 49 : 2, vol%) as molecular transporter to favor the Na^+ ion mobility, have been investigated through various techniques. The ionic conductivity was studied within the temperature range from 10 to 90 °C. The first measurement was performed at 40 °C and increased stepwise up to 90 °C. In the following cooling scan, the temperature was reduced stepwise down to 10 °C. The ionic conductivity (Fig. 4a) displays the Vogel–Tammann–Fulcher behavior, as commonly observed for Li and Na-based SIPEs.[39,40] This suggests that the Na^+ ion transport is supported by the motion of the anionic side chain in addition to the support of the molecular transporters (EC : DMC : FEC), facilitating the jump of the Na^+ ions between two anionic sites. The NaSTFSI-*co*-PET-MP/4A electrolyte exhibits an ionic conductivity of 1.4×10^{-5} S cm^{-1} at RT (20 °C), which increases with increasing temperature due to higher chain flexibility and ion mobility. The ionic conductivity reaches 1.3×10^{-4} S cm^{-1} at 90 °C, showing ionic conductivity comparable to that of other SIPEs blended with PVDF-HFP.[25,36,39] Additionally, the ionic conductivity values overlap those obtained in the first sweep, confirming the thermal reversibility of the NaSTFSI-*co*-PET-MP/4A electrolyte. Finally, the activation energy of NaSTFSI-*co*-PET-MP/4A electrolyte was calculated from the logarithm of the conductivity against 1000/T (see ESI, Fig. S3†). The NaSTFSI-*co*-PET-MP/4A electrolyte exhibits a low activation energy of 0.13 eV, which results in a fluent Na^+ ion transport as Na^+ ions require only minimal energy to hop from one ionic center to the next one.[41]

The electrochemical stability window of the NaSTFSI-*co*-PET-MP/4A electrolyte was investigated by LSV (Fig. 4b). The LSV measurements were carried out using two pristine cells to avoid cross-talking effects from the contamination of the decomposition products. Selecting the stability threshold at 5 μA cm^{-2} reveals a stability window up to 4.5 V *vs.* Na/Na^+ while no limitation is observed on the cathodic side prior to Na metal plating. This suggests that the designed NaSTFSI-*co*-PET-MP/4A electrolyte could be used with the most common sodium-based cathode materials, such as layered oxides and Prussian Blue analogues (PBAs).

The compatibility of the SIPE with the Na metal electrode was further investigated by stripping and plating tests (Fig. 4c)

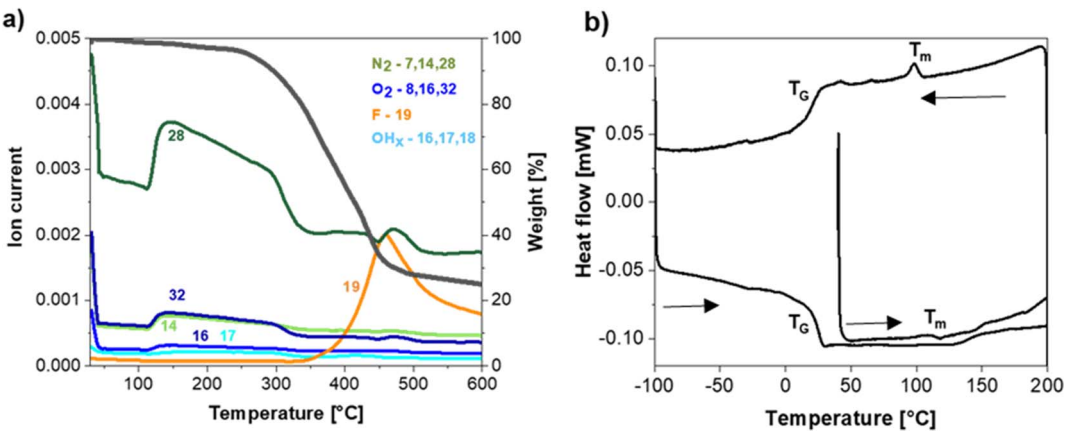

Fig. 3 (a) TGA/MS and (b) DSC of the NaSTFSI-*co*-PET-MP/4A membrane.

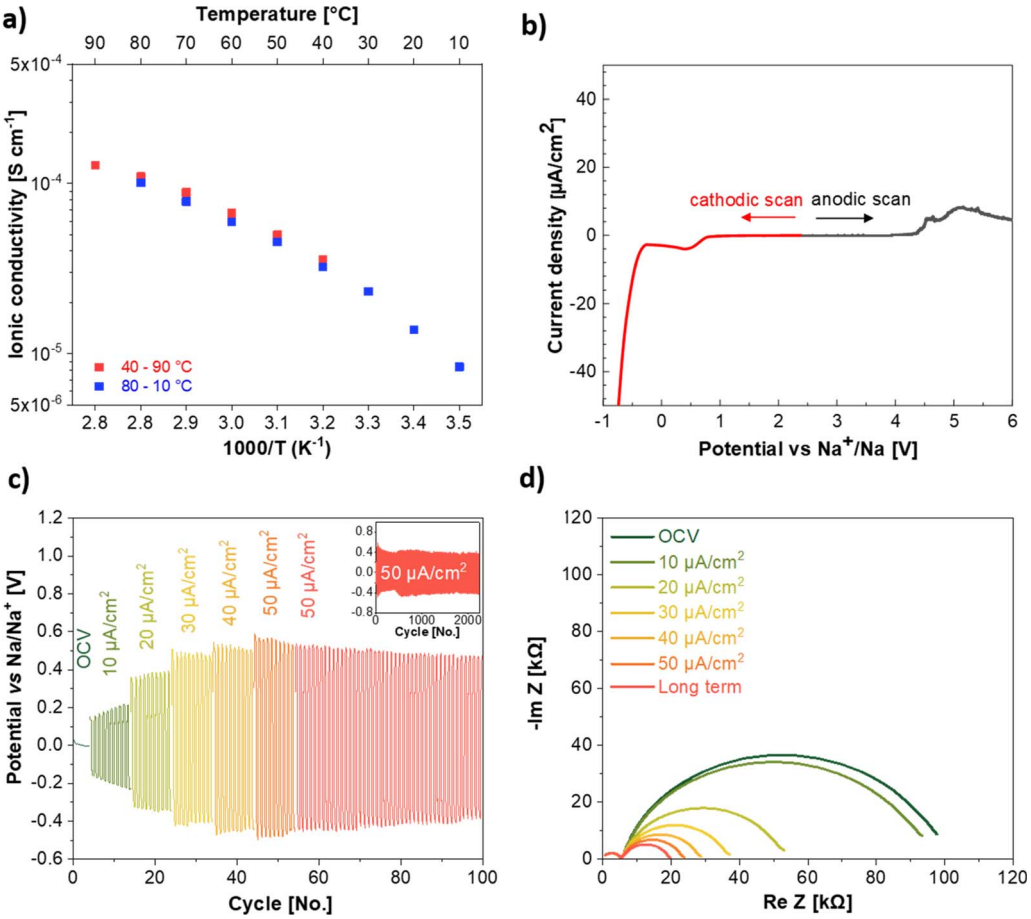

Fig. 4 Electrochemical characterization of NaSTFSI-*co*-PET-MP/4A electrolyte: (a) ionic conductivity in the temperature range of 10–90 °C; (b) anodic and cathodic scan in Na|Al cells; (c) Na stripping/plating test over 2000 h at different current densities in Na|Na symmetric cells, and (d) the corresponding Nyquist plot after cycling for 10 cycles at each current density. Additionally, the EIS was measured after 100 cycles at 50 μA cm^{-2} (red line). All tests were performed at 40 °C.

carried out at increasing current densities from 10 to 50 μA cm^{-2}. Following, prolonged cycling at 50 μA cm^{-2} was performed to investigate also the long-term stability of the NaSTFSI-*co*-PET-MP/4A electrolyte against Na metal. The tests show the expected increase of the overpotential with increasing current density. The observed overpotential of 0.15 V at 10 μA cm^{-2} increases to 0.35 V, 0.40 V, 0.41 V, and 0.42 V at 20, 30, 40, and 50 μA cm^{-2}, respectively. These values are comparable to those reported for other sodium-based SIPEs.[10] Additionally, the NaSTFSI-*co*-PET-MP/4A electrolyte showed stable behavior at all investigated current densities. Finally, the electrolyte could be cycled at 50 μA cm^{-2} for over 2000 cycles with a rather stable overpotential. Noteworthy, in the initial cycles after the EIS test and current density increase, a variation in the overpotential is observed (see inset Fig. 4c) due to a re-formation of the solid electrolyte interphase (SEI), which needs to be readapted. Nevertheless, after a few initial cycles, the overpotential stabilized, showing promising compatibility properties with Na metal for developing long-cycling quasi-solid-state sodium–metal cells.

The interface established by the NaSTFSI-*co*-PET-MP/4A electrolyte and the Na metal electrode was also investigated *via* EIS experiments. The Nyquist plots in Fig. 4d show the impedance spectra collected after the application of the different current densities and upon prolonged cycling. The ionic conductivity (first semicircle) does not change upon cycling; however, the second semicircle (charge transfer resistance at the Na metal/electrolyte interface) is reduced upon cycling. The NaSTFSI-*co*-PET-MP/4A electrolyte shows an initial (OCV) interface resistance of around 100 kΩ. After applying a current density of 10 μA cm^{-2}, the resistance slightly decreases, exhibiting about 95 kΩ. This reduction might be related to the SEI formation, which behaves as a "buffer" interlayer, facilitating the Na^+ ion transport across the solid–solid interface (further investigation in the section below). Indeed, the obtained impedance response and the size of the second semicircle are further reduced when cycling with 20 μA cm^{-2} for 10 cycles afterwards, suggesting the formation of a stable and probably homogeneous SEI, in agreement with the observed in the Na||Na symmetric stripping/plating test. The overall impedance and the size of the second semicircle are further reduced at each higher current density. This suggests that the formed SEI is growing and homogenizes with increasing current density to support the faster Na^+ ion diffusion and provide good compatibility between the NaSTFSI-*co*-PET-MP/4A electrolyte and Na metal and that the ion transport

in the SIPE is stable even at higher current densities. In addition, the stability of the formed SEI is further confirmed by measuring the impedance after cycling for an additional 100 cycles at 50 μA cm^{-2}, showing an even lower interface resistance of 20 kΩ (red line).

Study of the solid electrolyte interphase chemistry

EIS data reveals the formation of a stable SEI upon cycling. Hence, Na||Na symmetric cells after 5 cycles at 10 μA cm^{-2} were disassembled, and *ex situ* XPS analysis was performed on the surface of the NaSTFSI-*co*-PET-MP/4A electrolyte to identify the SEI chemistry. For the sake of comparison, XPS analysis was also performed on the dry NaSTFSI-*co*-PET-MP/4A membrane and the pristine NaSTFSI-*co*-PET-MP/4A electrolyte (soaked).

Fig. 5 illustrates the high-resolution C 1s, S 2p, and F 1s photoelectron spectra. In the C 1s spectra, five species are identified in the three investigated NaSTFSI-*co*-PET-MP/4A samples, which correspond to hydrocarbons (C–C, 284.8 eV), carbon–oxygen species (C–O_x, ~286 eV and ~287 eV), carbonates (CO_3, ~289 eV) and carbon–fluorine compounds (CF_x, ~290.5 eV),[42–44] in agreement with the O 1s region (ESI, Fig. S4†). The main component of the dry NaSTFSI-*co*-PET-MP/4A membrane corresponds to the hydrocarbon groups in the PETMP and PET4A blocks. The addition of EC : DMC : FEC to the membrane (soaked) results in an increase in the intensity of carbonates (CO_3) and CF_x species. The concentration of the carbon–oxygen species further increases after cycling, indicating the reduction of the molecular transporters, *e.g.*, EC, DMC, and FEC.[45]

The S 2p spectra display two main components, *i.e.*, S–C/S–H (~163 eV) and S–O_x (~168 eV) species, associated with the two monomers (NaSTFSI and PET4A).[44,46,47] The absence of other contributions suggests the stability of NaSTFSI and PET4A upon cycling. However, the F 1s spectra indicate the degradation of fluorine-containing components upon incorporation of the molecular transporters in the NaSTFSI-*co*-PET-MP/4A membrane. Considering that the S 2p spectra confirm the stability of sulfur species, it can be reasonably assumed that NaF (F 1s) formed as a result of FEC decomposition (poor thermal stability) and/or PVDF-HFP dehydrofluorination.[48,49] Upon cycling further, NaF formed from the decomposition of FEC as well as other fluorinated species, becoming the main fluorine-containing component of the SEI.[50] Its distribution along the SEI was further investigated by ToF-SIMS imaging, which was conducted across various surface areas of each sample. Fig. 6 (dried) shows the clear distribution of the NaSTFSI sodium salt monomer and PVDF-HFP along the dry NaSTFSI-*co*-PET-MP/4A membrane.

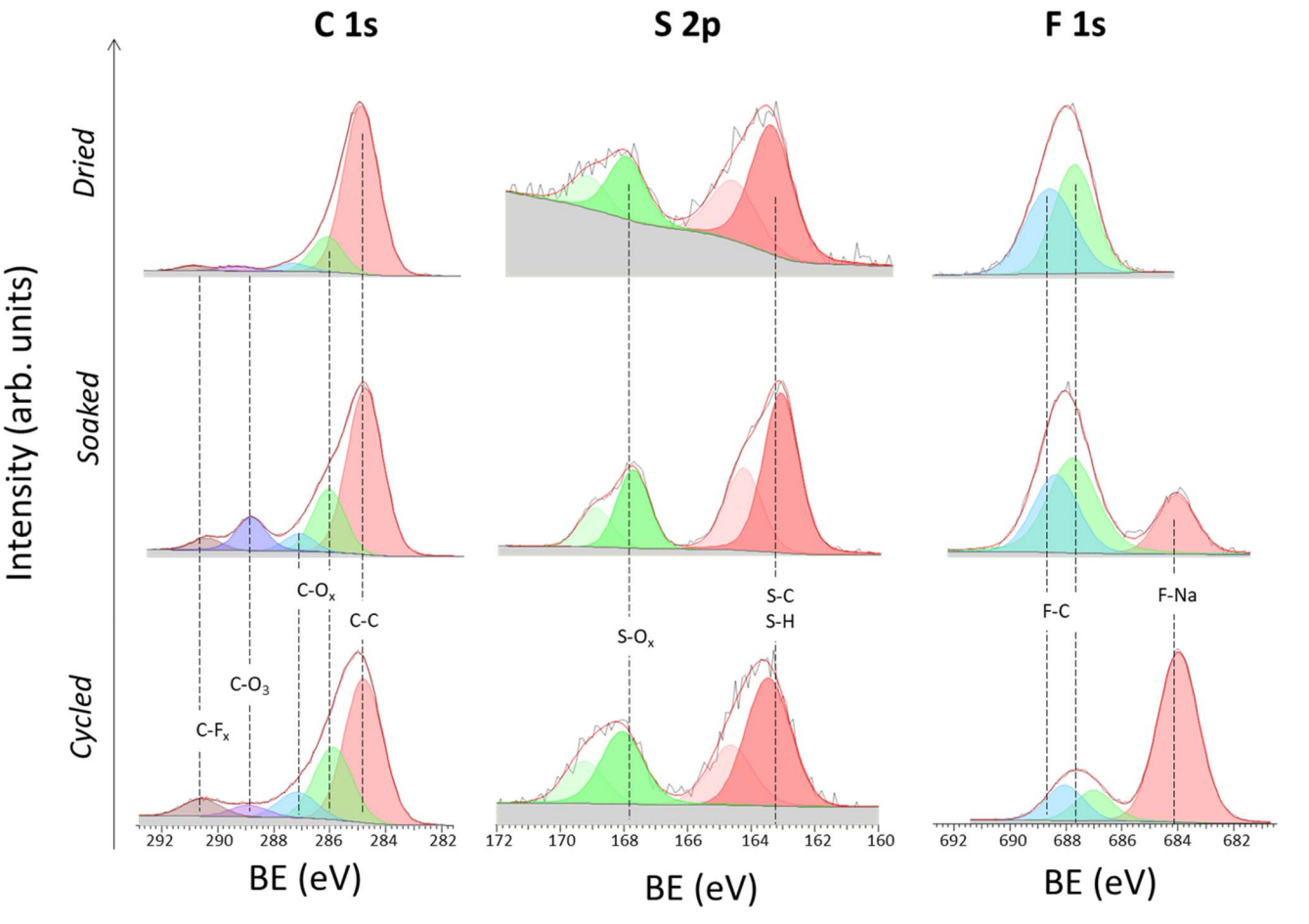

Fig. 5 *Ex situ* C 1s, S 2p, and F 1s XPS spectra of the surface of the NaSTFSI-*co*-PET-MP/4A membrane (dried), incorporating EC : DMC : FEC molecular transporters (soaked) and after cycling for 5 cycles in a Na|Na symmetric cell under 10 μA cm^{-2} (cycled).

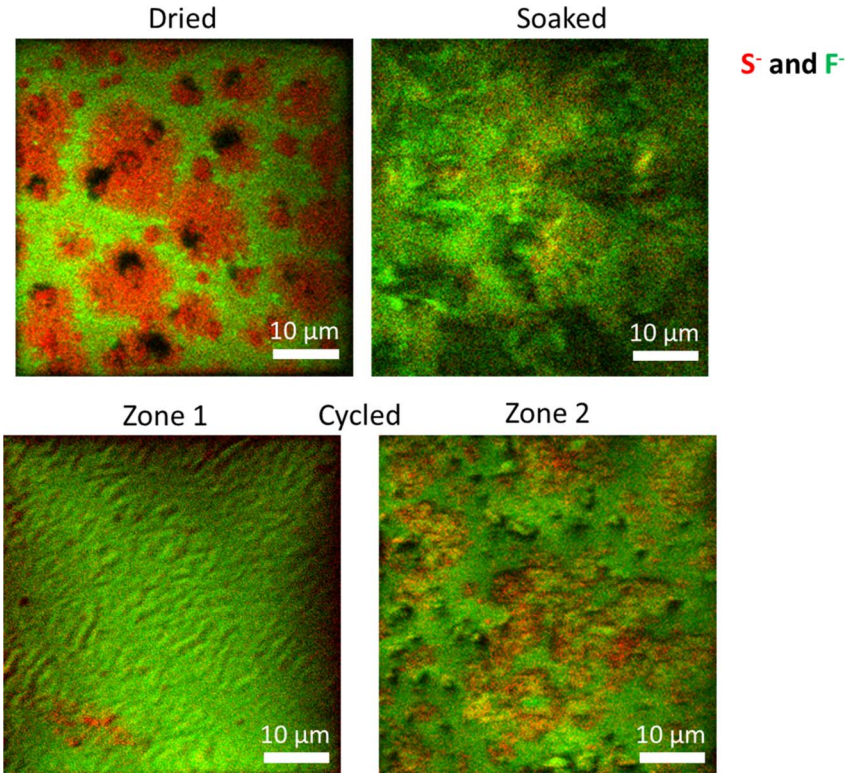

Fig. 6 ToF-SIMS combined mappings of S^- (red) and F^- (green) ionic fragments on the surface of the NaSTFSI-*co*-PET-MP/4A membrane (dried), incorporating EC : DMC : FEC molecular transporters (soaked) and after cycling for 5 cycles in a Na|Na symmetric cell under 10 µA cm^{-2} (cycled).

Once the EC : DMC : FEC molecular transporters are incorporated in the NaSTFSI-*co*-PET-MP/4A membrane, the surface is mainly covered by the fluorine species, mainly from FEC. After cycling, the surface of the NaSTFSI-*co*-PET-MP/4A electrolyte is still covered by fluorine species but, as indicated by the XPS investigation, mostly associated with NaF originating from the FEC's decomposition.[50]

The surface of cycled NaSTFSI-*co*-PET-MP/4A electrolyte has been investigated in two different regions (zone 1 and zone 2). Although both regions show high concentrations of fluorine species, the zone 2 mapping indicates larger areas with higher S-containing compounds. Nonetheless, NaF is also present, confirming the beneficial effect of FEC to induce the formation of a NaF-rich SEI and, thus, stabilizing the SEI and providing excellent compatibility to the NaSTFSI-*co*-PET-MP/4A electrolyte against Na metal.

Electrochemical performance of quasi-solid-state sodium–metal cells

The designed NaSTFSI-*co*-PET-MP/4A electrolyte was further investigated in proof of concept, quasi-solid-state sodium–metal cells employing PW as the cathode. Before assembling the quasi-solid-state sodium–metal cells, the PW electrodes were dried at 140 °C at 10^{-7} mbar to remove the water molecules and induce the formation of a phase transition from a hydrated to dehydrated rhombohedral crystal structure, finally obtaining a chemical composition of $Na_2Fe[Fe(CN)_6]$. It was observed that PW electrodes dried in mild conditions, such as 140 °C at 10^{-3} mbar, maintained the water molecules, resulting in a low specific capacity for delivery (ESI, Fig. S5†).

The collected voltage profiles and the specific capacity upon cycling of PW||1 M $NaPF_6$ in EC : DEC (3 : 7 vol%)||Na cells are illustrated in Fig. 7a and b, respectively. In this electrolyte, the voltage profile of rhombohedral PW shows two plateaus at 3.0 and 3.3 V *vs.* Na/Na^+. The initial charge and discharge capacity of PW were 154 and 160 mA h g^{-1}, respectively, at 0.02C. The specific capacity decayed slightly upon cycling by increasing the current from 0.02C to 0.03C and 0.1C, but the cell showed a specific capacity of 150 mA h g^{-1} and a Coulombic efficiency above 99% after 40 cycles.

The voltage profiles of the PW tested with NaSTFSI-*co*-PET-MP/4A electrolyte (Fig. 7c) show also two voltage plateaus upon both the charge and the discharge. However, due to the lowest NaSTFSI-*co*-PET-MP/4A electrolyte ionic conductivity, the quasi-solid-state sodium–metal cell exhibited high polarizations and sloping plateaus. The initial charge and discharge curves show a noisy signal due to side reactions and the corresponding SEI formation, as observed by XPS and ToF-SIMS experiments. Indeed, this is in agreement with the lower initial Coulombic efficiency. The noisy signal upon discharge could also be attributed to soft Na dendrites formation, which cannot be excluded. The observed overpotential of 0.4 V was expected considering the Na||Na symmetric stripping plating test. In addition, a similar overpotential was observed when PW||Na cell was tested with NaFSI in poly(trimethylene carbonate) (PTMC) polymer electrolyte.[51] However, the large polarization does not influence the specific capacity of the quasi-

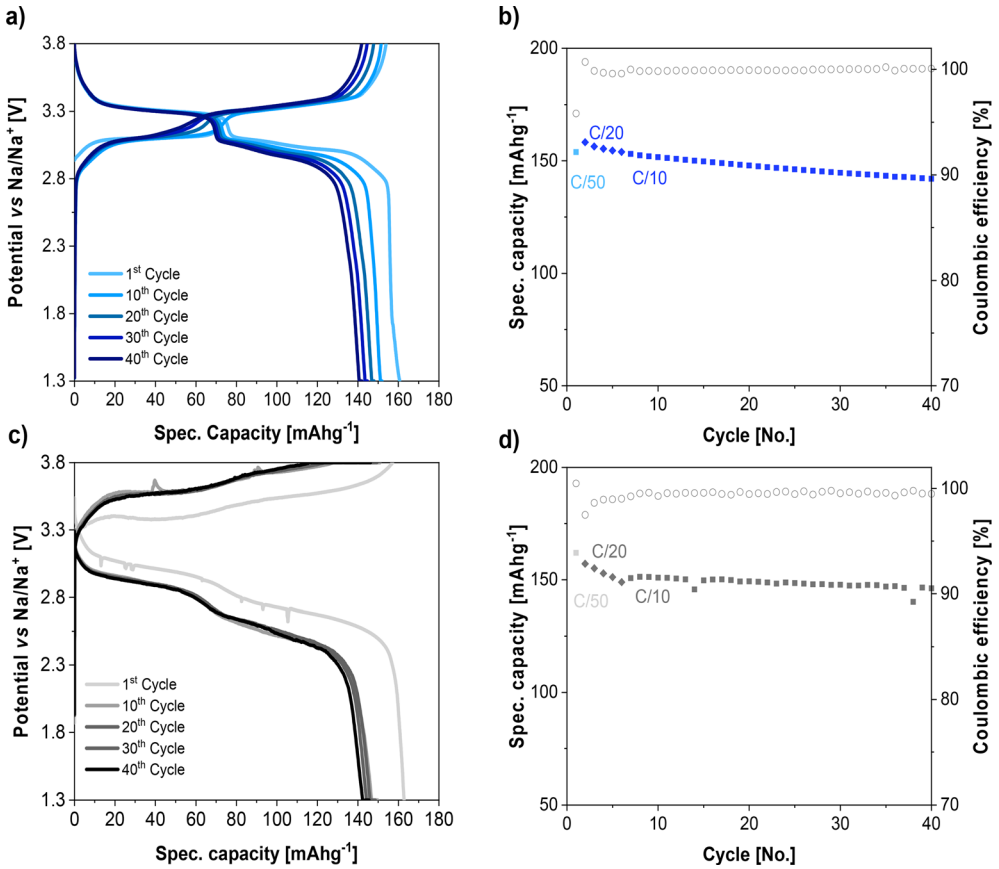

Fig. 7 Voltage profile and cycling performance of PW cathode using (a and b) 1 M $NaPF_6$ in EC : DEC (3 : 7 vol%) liquid electrolyte and (c and d) NaSTFSI-*co*-PET-MP/4A electrolyte at 40 °C.

solid-state sodium–metal cell, where the initial charge and discharge capacity of the PW at 0.02C correspond to 163 and 162 mA h g^{-1}, respectively, which are similar to those obtained in liquid cells. The cell capacity slightly dropped to 150 mA h g^{-1} and 147 mA h g^{-1} when increasing the current to 0.03C and 0.1C, respectively. However, although the capacity decays in the first cycles at 0.2C, after 5 cycles, the capacity and Coulombic efficiency remain constant, delivering a capacity retention of 98% after 40 cycles. This might be due to the stabilization of the SEI, as observed in the Na||Na symmetric cells. These preliminary results indicated the suitability of the designed NaSTFSI-*co*-PET-MP/4A electrolyte for quasi-solid-state sodium-based batteries.

Conclusion

In this work, a new, three-dimensional, single-ion conducting polymer electrolyte (NaSTFSI-*co*-PET-MP/4A), consisting of in-house synthesized NaSTFSI, and PEMTP, PET4A, and PVDF-HFP, was manufactured into self-standing and flexible single-ion conducting polymer electrolyte membranes. The physico-chemical properties of the NaSTFSI salt monomer and NaSTFSI-*co*-PET-MP/4A electrolyte were investigated through NMR, CPMAS-NMR, and FT-IR, also confirming the highly interconnected three-dimensional structure of the polymer. The NaSTFSI-*co*-PET-MP/4A electrolyte containing 50 wt% of molecular transporters exhibits thermal stability up to 280 °C, electrochemical stability up to 4.5 V *vs.* Na/Na^+, and ionic conductivity of 1.3×10^{-4} S cm^{-1} at 90 °C and 1.4×10^{-5} S cm^{-1} at RT. The NaSTFSI-*co*-PET-MP/4A electrolyte shows highly stable cycling behavior against Na metal (more than 2000 h at 50 μA cm^{-2} and 40 °C) due to the formation of a stable NaF-rich SEI, confirmed by EIS, XPS, and ToF-SIMS. Furthermore, PW||NaSTFSI-*co*-PET-MP/4A||Na quasi-solid-state sodium–metal cells operating at 40 °C deliver a specific capacity of 147 mA h g^{-1} at 0.1C with excellent Coulombic efficiency. These results validate the potential of designed sodium-based single-ion conductive polymer electrolytes for the next generation of sodium-based batteries.

Data availability

The authors are available to provide data upon request.

Author contributions

C. W.: investigation, methodology, data analysis, visualization, writing—original draft & editing. T.-L. L.: ToF-SIMS experiments, data analysis, visualization, review. E. S.: ssNMR experiments, data analysis, writing – original draft & review. T. G.: visualization, review. E. D. V.: XPS experiments, data analysis, visualization, review. G. B.: visualization, review. M. Z.: conceptualization, methodology, investigation, formal analysis,

project administration, supervision, writing – review and editing. S. P.: conceptualization, methodology, investigation, formal analysis, funding acquisition, project administration, supervision, writing—review and editing.

Conflicts of interest

The authors declare no conflicts of interest.

Acknowledgements

This work was funded by the HORIZON 2020 program (Project "SIMBA" 963542). The authors thank the Helmholtz Association for financial support. The von Delius group at Ulm University is acknowledged for the solution NMR measurements. Altris AB is acknowledged for providing the Prussian White cathode. C. W. and M. Z. are grateful to Dr Matilda Folkenant and Dr William Brant for the insightful discussions.

References

1 I. Hasa, S. Mariyappan, D. Saurel, P. Adelhelm, A. Y. Koposov, C. Masquelier, L. Croguennec and M. Casas-Cabanas, *J. Power Sources*, 2021, **482**, 228872.
2 P. K. Nayak, L. Yang, W. Brehm and P. Adelhelm, *Angew. Chem., Int. Ed.*, 2018, **57**, 102–120.
3 X. Wang, S. Roy, Q. Shi, Y. Li, Y. Zhao and J. Zhang, *J. Mater. Chem. A*, 2021, **9**, 1938–1969.
4 W. Lu, Z. Wang and S. Zhong, *J. Phys.: Conf. Ser.*, 2021, **2109**, 012004.
5 C. Ruiz, *et al.*, *Sodium-ion batteries ready for commercialisation: for grids, homes, even compact EVs*, energypost.eu, 2023, **https://energypost.eu/sodium-ion-batteries-ready-for-commercialisation-for-grids-homes-even-compact-evs/**.
6 Y. Lu, L. Li, Q. Zhang, Z. Niu and J. Chen, *Joule*, 2018, **2**, 1747–1770.
7 C. Cao, W. Liu, L. Tan, X. Liao and L. Li, *Chem. Commun.*, 2013, **49**, 11740.
8 S. Chen, J. Ishii, S. Horiuchi, M. Yoshizawa-Fujita and E. Izgorodina, *Phys. Chem. Chem. Phys.*, 2017, **19**, 17366–17372.
9 Y. Wang, S. Song, C. Xu, N. Hu, J. Molenda and L. Lu, *Nano Mater. Sci.*, 2019, **1**, 91–100.
10 X. Dong, X. Liu, H. Li, S. Passerini and D. Bresser, *Angew. Chem., Int. Ed.*, 2023, **62**, e202308699.
11 W. Gorecki, M. Jeannin, E. Belorizky, C. Roux and M. Armand, *J. Phys.: Condens.Matter*, 1995, **7**, 6823–6832.
12 A. Hosseinioun, P. Nürnberg, M. Schönhoff, D. Diddens and E. Paillard, *RSC Adv.*, 2019, **9**, 27574–27582.
13 K. M. Abraham, H. S. Choe and D. M. Pasquariello, *Electrochim. Acta*, 1998, **43**, 2399–2412.
14 J. Zheng, W. li, X. Liu, J. Zhang, X. Feng and W. Chen, *Energy Environ. Mater.*, 2023, **6**, e12422.
15 D. Kumar and S. A. Hashmi, *J. Power Sources*, 2010, **195**, 5101–5108.
16 L. Qiao, X. Judez, T. Rojo, M. Armand and H. Zhang, *J. Electrochem. Soc.*, 2020, **167**, 070534.
17 D. Roscher, Y. Kim, D. Stepien, M. Zarrabeitia and S. Passerini, *Batteries Supercaps*, 2023, **6**, e202300092.
18 D. Morales, L. Gomes Chagas, D. Paterno, S. Greenbaum, S. Passerini and S. Suarez, *Electrochim. Acta*, 2021, **377**, 138062.
19 K. Timachova, H. Watanabe and N. P. Balsara, *Macromolecules*, 2015, **48**, 7882–7888.
20 C. Li, B. Qin, Y. Zhang, A. Varzi, S. Passerini, J. Wang, J. Dong, D. Zeng, Z. Liu and H. Cheng, *Adv. Energy Mater.*, 2019, **9**, 1803422.
21 Y. S. Zhu, X. J. Wang, Y. Y. Hou, X. W. Gao, L. L. Liu, Y. P. Wu and M. Shimizu, *Electrochim. Acta*, 2013, **87**, 113–118.
22 X.-G. Sun and J. B. Kerr, *Macromolecules*, 2006, **39**, 362–372.
23 J. L. Olmedo-Martínez, A. Fdz De Anastro, M. Martínez-Ibañez, A. J. Müller and D. Mecerreyes, *Energy Fuels*, 2023, **37**, 5519–5529.
24 L. Yang, Y. Jiang, X. Liang, Y. Lei, T. Yuan, H. Lu, Z. Liu, Y. Cao and J. Feng, *ACS Appl. Energy Mater.*, 2020, **3**, 10053–10060.
25 S. Das, S. Jana, M. Orságh, K. By's, J. Mishra, M. Uchman and V. Adyam, *ACS Appl. Energy Mater.*, 2023, **6**, 5113–5121.
26 J. Li, H. Zhu, X. Wan, M. Armand, D. R. MacFarlane and M. Forsyth, *Electrochim. Acta*, 2015, **175**, 232–239.
27 E. Šić, J. Rohrer, E. III Ricohermoso, K. Albe, E. Ionescu, R. Riedel, H. Breitzke, T. Gutmann and G. Buntkowsky, *ChemSusChem*, 2023, **16**, e202202241.
28 I. Scholz, P. Hodgkinson, B. H. Meier and M. Ernst, *J. Chem. Phys.*, 2009, **130**, 114510.
29 G. Socrates, *Infrared and Raman Characteristic Group Frequencies: Tables and Charts*, John Wiley & Sons, 2004.
30 Y. Zhong, L. Zhong, S. Wang, J. Qin, D. Han, S. Ren, M. Xiao, L. Sun and Y. Meng, *J. Mater. Chem. A*, 2019, **7**, 24251–24261.
31 M. T. Gokmen, J. Brassinne, R. A. Prasath and F. E. Du Prez, *Chem. Commun.*, 2011, **47**, 4652.
32 S. Kuypers, S. Kumar Pramanik, L. D'Olieslaeger, G. Reekmans, M. Peters, J. D'Haen, D. Vanderzande, T. Junkers, P. Adriaensens and A. Ethijaran, *Chem. Commun.*, 2015, **51**, 15858–15861.
33 K. Schmidt-Rohr and H. Wolfgang Spiess, *Multidimensional Solid-State NMR and Polymers*, Elsevier, 2012.
34 C. Hucher, F. Beaume, R.-P. Eustache and P. Tekely, *Macromolecules*, 2005, **38**, 1789–1796.
35 S. Ferrari, E. Quartarone, P. Mustarelli, A. Magistris, M. Fagnoni, S. Protti, C. Gerbaldi and A. Spinella, *J. Power Sources*, 2010, **195**, 559–566.
36 R. Meziane, J.-P. Bonnet, M. Courty, K. Djellab and M. Armand, *Electrochim. Acta*, 2011, **57**, 14–19.
37 D. J. Blundell, *Polymer*, 1987, **28**, 2248–2251.
38 K. Ishino, H. Shingai, Y. Hikita, I. Yoshikawa, H. Houjou and K. Iwaswe, *ACS Omega*, 2021, **6**, 32869–32878.
39 H. Guan, Z. Guo, J. Ding and F. Lian, *J. Appl. Polym. Sci.*, 2016, **133**, 43510.
40 S. Das and A. Ghosh, *Electrochim. Acta*, 2015, **171**, 59–65.
41 J. Baek, B. Yoon, H. Jeong, J. Jeong, S. Mamidi, H.-K. Seo, C.-R. Lee and I. Seo, *J. Electroanal. Chem.*, 2022, **920**, 116631.

42 M. C. Biesinger, *Appl. Surf. Sci.*, 2022, **597**, 153681.
43 A. Gulino, F. Lupo, G. G. Condorelli, M. E. Fragalá, M. E. Amato and G. Scarlata, *J. Mater. Chem.*, 2008, **18**, 5011.
44 G. Beamson and D. Briggs, High Resolution XPS of Organic Polymers, *The Scienta ESCA300 Database*, John Wiley & Sons Ltd, Chichester, UK, 1992.
45 V. Simone, L. Lecarme, L. Simonin and S. Martinet, *J. Electrochem. Soc.*, 2017, **164**, A145–A150.
46 F. Buchner, M. Bozorgchenani, B. Uhl, H. Farkhondeh, J. Bansmann and R. J. Behm, *J. Phys. Chem. C*, 2015, **119**, 16649–16659.
47 Y. Peng, R. Badam, T. P. Jayakumar, W. Wannapakdee, C. Cahngtong and N. Matsumi, *J. Electrochem. Soc.*, 2022, **169**, 050515.
48 A. J. Dias and T. J. McCarthy, *J. Polym. Sci., Polym. Chem. Ed.*, 1985, **23**, 1057–1061.
49 M. A. Muñoz-Márquez, M. Zarrabeitia, E. Castillo-Martínez, A. Eguia-Barrio, T. Rojo and M. Casas-Cabanas, *ACS Appl. Mater. Interfaces*, 2015, **7**, 7801–7808.
50 H. Kumar, E. Detsi, D. P. Abraham and V. B. Schenoy, *Chem. Mater.*, 2016, **24**, 8930–8941.
51 C. Sångeland, R. Mogensen, D. Brandell and J. Mindemark, *ACS Appl. Polym. Mater.*, 2019, **1**, 825–832.